



OPEN

Quantifying lumbar vertebral perfusion by a Tofts model on DCE-MRI using segmental versus aortic arterial input function

Yi-Jui Liu^{1,2}, Hou-Ting Yang^{3,4}, Melissa Min-Szu Yao^{5,6}, Shao-Chieh Lin³, Der-Yang Cho⁷, Wu-Chung Shen^{8,9}, Chun-Jung Juan^{8,9,10}✉ & Wing P. Chan^{5,6}✉

The purpose of this study was to investigate the influence of arterial input function (AIF) selection on the quantification of vertebral perfusion using axial dynamic contrast-enhanced magnetic resonance imaging (DCE-MRI). In this study, axial DCE-MRI was performed on 2 vertebrae in each of eight healthy volunteers (mean age, 36.9 years; 5 men) using a 1.5-T scanner. The pharmacokinetic parameters K^{trans} , v_e , and v_p , derived using a Tofts model on axial DCE-MRI of the lumbar vertebrae, were evaluated using various AIFs: the population-based aortic AIF (AIF_PA), a patient-specific aortic AIF (AIF_A) and a patient-specific segmental arterial AIF (AIF_SA). Additionally, peaks and delay times were changed to simulate the effects of various AIFs on the calculation of perfusion parameters. Nonparametric analyses including the Wilcoxon signed rank test and the Kruskal–Wallis test with a Dunn–Bonferroni post hoc analysis were performed. In simulation, K^{trans} and v_e increased as the peak in the AIF decreased, but v_p increased when delay time in the AIF increased. In humans, the estimated K^{trans} and v_e were significantly smaller using AIF_A compared to AIF_SA no matter the computation style (pixel-wise or region-of-interest based). Both these perfusion parameters were significantly greater using AIF_SA compared to AIF_A.

Abbreviations

AIF	Arterial input function
AIF_A	Patient-specific aortic AIF
AIF_PA	Population-based aortic AIF
AIF_SA	Patient-specific segmental arterial AIF
DCE-MRI	Dynamic contrast-enhanced magnetic resonance imaging
KWT	Kruskal–Wallis test
PWM	Pixelwise method
RBM	ROI-based method
SA	Segmental artery
SNR	Signal-to-noise ratio
WSRT	Wilcoxon signed rank test

¹Department of Automatic Control Engineering, Feng Chia University, Taichung, Taiwan. ²Master's Program of Biomedical Informatics and Biomedical Engineering, Feng Chia University, Taichung, Taiwan. ³Ph.D. Program in Electrical and Communication Engineering in Feng Chia University, Taichung, Taiwan. ⁴Department of Nuclear Medicine, Chang Gung Memorial Hospital, Keelung, Taiwan. ⁵Department of Radiology, Wan Fang Hospital, Taipei Medical University, 111 Hsing-Long Road, Section 3, Taipei 116, Taiwan. ⁶Department of Radiology, School of Medicine, College of Medicine, Taipei Medical University, Taipei, Taiwan. ⁷Department of Neurosurgery, China Medical University Hospital, Taichung, Taiwan. ⁸Department of Radiology, School of Medicine, College of Medicine, China Medical University, Taichung, Taiwan. ⁹Department of Medical Imaging, China Medical University Hospital, Taichung, Taiwan. ¹⁰Department of Medical Imaging, China Medical University Hsinchu Hospital, Hsinchu, 199, Sec. 1, Xinglong Rd., Zhubei City, Hsinchu County 302, Taiwan. ✉email: peterjuancj@yahoo.com.tw; wingchan@tmu.edu.tw

Dynamic contrast-enhanced magnetic resonance imaging (DCE-MRI) exploits tissue perfusion properties via quantitative analysis using appropriate tracer kinetics models¹. Bone perfusion involves a blood circulation process which comprises several factors such as blood flow, capillary capacitance, permeability, interstitial space volume, interstitial diffusion, and venous return².

Since 1991, DCE-MRI has been widely used *in vivo*. For example, bone marrow perfusion of the proximal femur was evaluated in a dog model by Cova et al.³. In 1995, Fujisawa et al. demonstrated vascular ingrowth after surgery in avascular necrosis of the femoral head⁴. In tumor studies, the perfusion of benign and malignant lesions in bone marrow^{5–8} and in lymphoproliferative diseases with diffuse bone marrow involvement⁹ has been investigated, and responses to chemotherapy have been monitored¹⁰. In the human spine, disc degeneration has been correlated with low vertebral perfusion, and an inverse association between vertebral perfusion and age has been demonstrated¹¹. Maximal vertebral enhancement and the enhancement slope have been shown to decrease in those with osteopenia or osteoporosis^{12,13}. Moreover, DCE-MRI outperforms conventional MRI in discriminating hypervascular from hypovascular spinal metastases¹⁴.

A two-compartment model has been most often used for quantitative analyses measuring the vertebral marrow perfusion. A tracer kinetic analysis¹ produces four perfusion parameters: K^{trans} , the efflux rate of gadolinium contrast from blood plasma to the extracellular extravascular space (EES); K_{ep} , the rate constant for the return from the EES into the blood plasma; v_e , the extracellular extravascular volume fraction; and v_p , the volume fraction. Arterial input function (AIF) obtained from the tracer time curve for the aorta has been applied in quantitative perfusion models used in vertebral studies^{15–17}. Whether the aorta is the only choice for AIF in vertebral perfusion studies is debatable. In humans, each vertebral body is supplied directly by a pair of segmental arteries arising from the aorta^{18,19}. It is plausible that AIF obtained from the patient-specific segmental artery (AIF_SA) is less biased than AIF obtained from the patient-specific aorta (AIF_A) when using DCE-MRI for quantifying vertebral perfusion. To the best of our knowledge, lumbar perfusion using AIF_SA on DCE-MRI has not yet been documented.

We hypothesized that the amplitude and phase of AIF_SA differ from those of AIF_A and that perfusion parameters computed based on AIF_SA differ from those based on AIF_A. The aim of this study was to verify the effects of AIF amplitude and phase on perfusion parameters in simulation and to examine the differences in lumbar vertebral perfusion parameters computed based on the AIF_SA compared to AIF_A using axial DCE-MRI.

Materials and methods

All experiments and methods were carried out in compliance with relevant guidelines and regulations. All experimental protocols were approved by the Institutional Review Board of Wan Fang Hospital. Written informed consent was obtained from each participant. A total of eight healthy volunteers (mean age 36.9 years; range 23–64 years; 5 male) were enrolled in this prospective study. Enrollment was limited to eight to minimize risks associated with the intravenous injection of gadolinium-based contrast agent, as mentioned elsewhere²⁰.

MRI protocols. All MR scans were performed using a clinical whole-body scanner with 1.5-T magnetic field strength (Avanto, Siemens, Erlangen, Germany). To identify the location of the segmental arteries, a 3-D TrueFISP non-contrast magnetic resonance angiography was acquired on the coronal plane covering the entire vertebral body using the following parameters: slice thickness, 2 mm; field-of-view, 360 × 360 mm; matrix size, 256 × 256; repetition time(TR)/echo time (TE), 508.9 ms/1.5 ms; and flip angle, 80°. Two axial planes of the lumbar vertebrae along the course of the segmental arteries at L1 and L2 were identified (Fig. 1). Then, axial T1 measures and DCE-MRI were performed, applying identical settings for field-of-view (30 × 30 cm), matrix size (256 × 250), and slice thickness (10 mm). Gradient echo images using a fast low angle shot (FLASH) sequence with a TR/TE of 19 ms/4 ms, and flip angles of 5°, 10°, 20°, 40°, 60°, and 80° were acquired to calculate T1. Using another FLASH sequence at the same TR/TE but a flip angle of 40°, another DCE-MRI was acquired, achieving more T1-weighted images via gradient echo sequences and obtaining a greater SNR for measuring T1 compared to what could be obtained using a smaller flip angle. A parallel imaging technique (GeneRalized Autocalibrating Partially Parallel Acquisitions; GRAPPA) was used, applying to dynamic scans an acceleration factor of 2 and a partial Fourier acquisition along the phase encoding direction with a factor of 6/8, netting 1.8 s (19 ms × 250 × (6/8)/2) to complete a dynamic scan. The temporal resolution was 2 s when two axial slices were acquired within one TR interval. Total acquisition time was 7 min and 20 s. A pre-saturation band with parallel slices was applied to the upstream aorta to eliminate the in-flow pulsation. An auto-injector was used to administer a bolus injection of Gd-DOTA (total dose, 0.1 mmol/kg) followed by a 10-ml saline flush via an arm vein at a rate of 2 ml/s.

Data analysis. *MR signal to concentration of contrast agent.* Post-processing of the simulated data and MRI images was performed using in-house software implemented in MATLAB (The MathWorks Inc., Natick, MA), then T1 maps were calculated using the variable flip angle T1 measures (Fig. 2)²¹. The signal of a gradient echo using a spoiled gradient is:

$$S = \frac{M_0 \sin \alpha (1 - e^{-TR/T_1})}{1 - \cos \alpha e^{-TR/T_1}} e^{-TE/T_2^*}, \quad (1)$$

where M_0 is the equilibrium magnetization, and α is the excitation flip angle. The concentration of contrast agent was transformed from the MR signal based on the T1 relaxation rate:

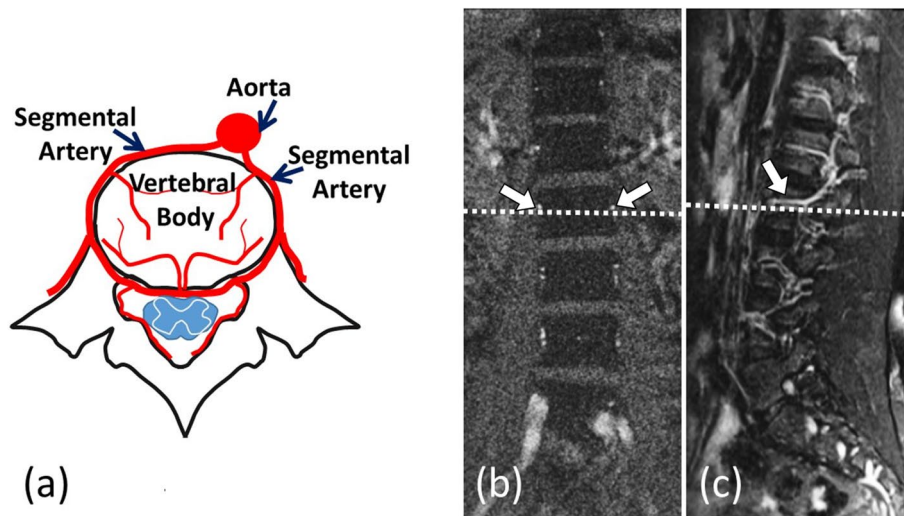


Figure 1. (a) The anatomic relationships between a lumbar vertebral body and its supplying arteries, including the abdominal aorta and segmental arteries. The axial plane through the L1 segmental arteries (just above the dotted lines) was selected on coronal (b) and sagittal (c) images of magnetic resonance angiography. White arrows indicate the segmental arteries.

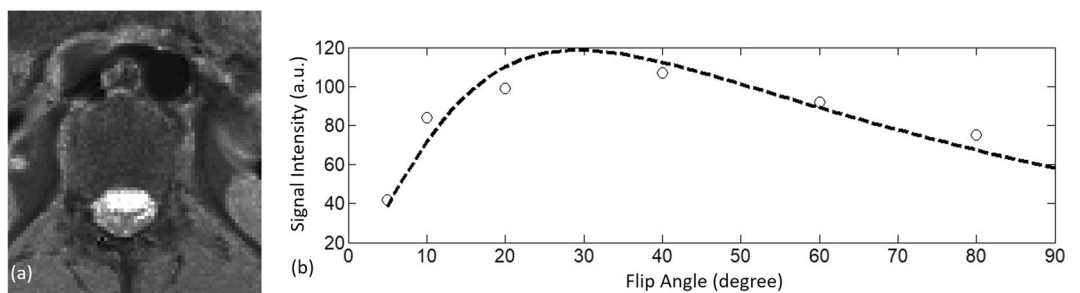


Figure 2. A T1 map (a) was generated from a pixel-by-pixel curve fitting of a signal-intensity-flip-angle curve (b).

$$C(t) = \frac{1}{r_1} \left(\frac{1}{T_1(t)} - \frac{1}{T_{10}} \right), \tag{2}$$

where $C(t)$ is the concentration of the contrast agent during DCE-MRI, r_1 is the relaxation rate for the contrast agent ($3.6 \text{ s}^{-1} \text{ mmol}^{-1}$)²², $T_1(t)$ is the T1 value during DCE-MRI, and T_{10} is the pre-contrast T1 value, as obtained in Eq. (1). Based on Eq. (1), the relationships between the dynamic MR signal, the initial MR signal, and the T1 relaxation rate in a gradient echo with a spoiled gradient is:

$$\frac{S(t)}{S_0} = \frac{(1 - e^{-TR/T_1(t)})}{1 - \cos \alpha e^{-TR/T_1(t)}} \frac{1 - \cos \alpha e^{-TR/T_{10}}}{(1 - e^{-TR/T_{10}})}. \tag{3}$$

Theoretically, because the time-invariant terms including $(M_0 \sin \alpha)$ and (e^{-TE/T_2^*}) in Eq. (1) were cancelled, the signal ratio $(S(t)/S_0)$ will be less influenced by the T2* term. Therefore, the concentration of the contrast agent can be calculated by substituting of T_{10} and $T_1(t)$, obtained from Eqs. (1) and (3), into Eq. (2).

Pharmacokinetic modelling. In this study, the analysis of the DCE-MRI data was based on a modified Tofts model^{23,24} that assumes the contrast media reaches an equilibrium between the plasma and the EES via an iso-directional permeability described below:

$$C_t(t) = v_p C_p(t) + C_p(t) \otimes K^{trans} \exp(-K^{trans} t/v_e), \tag{4}$$

where $C_t(t)$ denotes the contrast concentration in tissue, v_p denotes the fractional plasma volume, $C_p(t)$ denotes the contrast concentration in the plasma for the AIF, K^{trans} denotes the transfer constant (from plasma into EES), and v_e denotes the fractional volumes of EES per unit volume of tissue. Note that $K^{trans}/v_e = k_{ep}$, the reflux rate, and

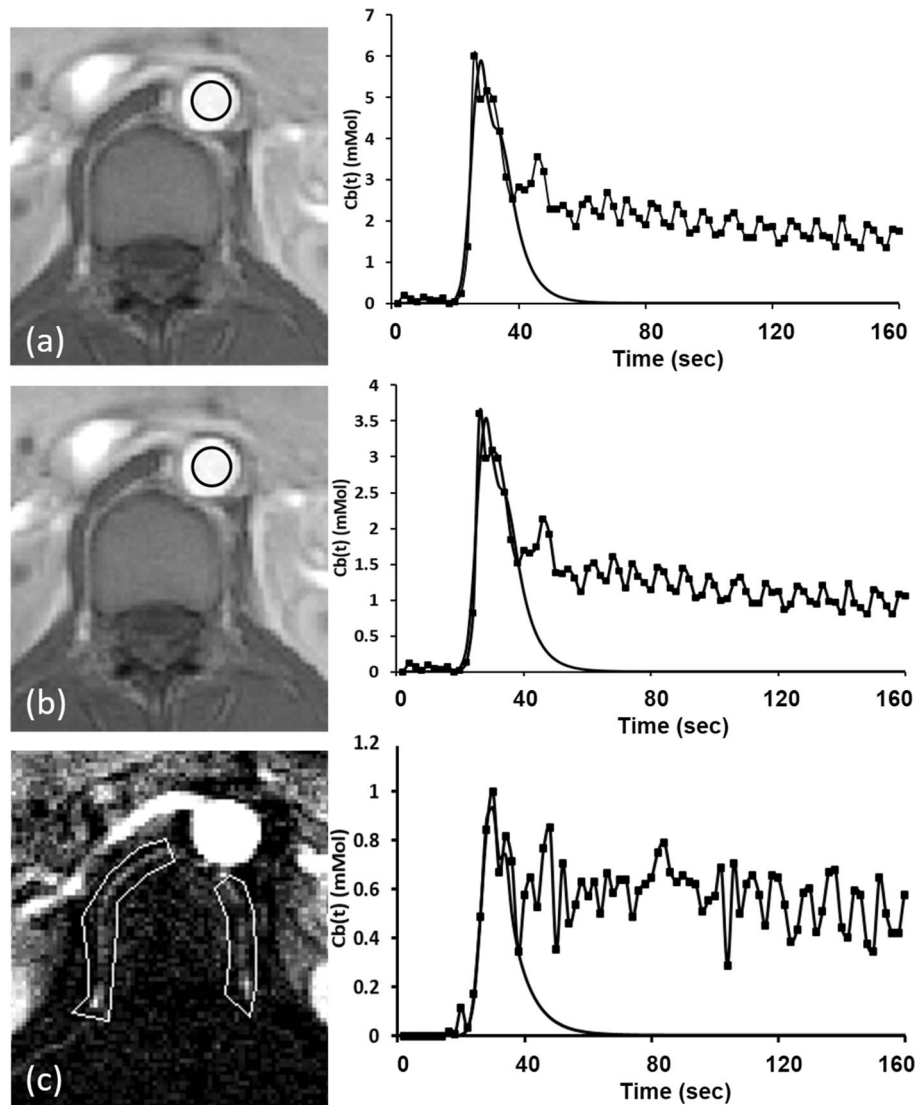


Figure 3. Selecting the region of interest for the aorta, using the peak contrast concentration in the population blood (a) or the individual blood concentration (b) and for the segmental arteries (c). Each is accompanied by its mean concentration time curves (solid line; squares indicate data points) and arterial input functions (solid line alone), fitted using a mixture between a Gaussian function and an exponential function modulated by a sigmoid function.

the plasma concentration of the AIF (C_p) is calculated as the concentration time curve of AIF ($C_b(t)$) multiplied by $1/(1 - \text{Hct})$, where Hct (hematocrit) is 0.42²⁵.

Vertebral perfusion was quantified on a pixel-by-pixel basis using regions of interest (ROIs) that contour the entire vertebral body and arteries selected for calculating AIF, respectively. Perfusion parametric maps were constructed using a deconvolution method based on a nonlinear least-squares fitting^{26–29}. Perfusion parametric maps of the vertebra constructed by using AIF_A and AIF_SA were generated based on a pixel-wise method (PWM) and an ROI-based method (RBM) for comparison.

AIF selection. The manually selected ROIs of the segmental arteries and aorta together with their corresponding concentration time curves and curve-fitted AIFs are shown in Fig. 3. To minimize the influence of the partial volume effects on the segmental artery, subtracted dynamic images were generated by subtracting each dynamic image from the average across the first 5 phases of the dynamic images, obviously highlighting and clearly distinguishing the segmental arteries from the surrounding static tissue (Fig. 3c). The segmental artery on either side was then segmented by manually contouring an ROI on the subtracted dynamic images, encompassing that artery. The signal time curve was plotted for each pixel within that ROI, and the pixel with the maximal peak value was automatically chosen. Finally, AIF_SA was computed from the concentration time curve of that pixel. On the other hand, AIF_A was computed from the concentration time curve of the aortic ROI, obtained by manually placing a circular ROI within the aorta. For comparison, the aortic time curve was transformed into

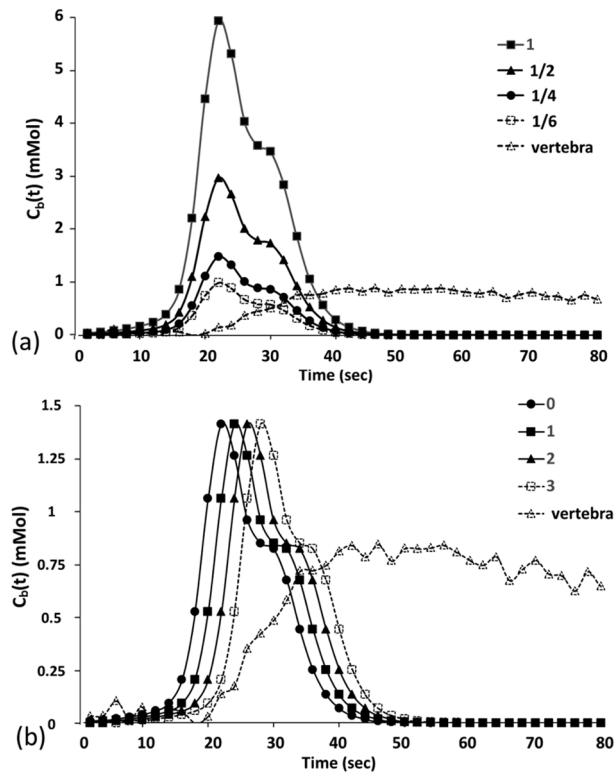


Figure 4. Simulation of arterial and vertebral concentration time curves generated using a typical aortic concentration time curve sample for one participant, showing the peak scaled by 1, 1/2, 1/4, and 1/6 (a) and the delay time adjusted by 0, 1, 2, and 3 time points (b). The first 80 of 440 s are shown.

a population-based time curve, from which the AIF_PA, also known as the Parker AIF (6 mmol in blood concentration)^{25,30}, was generated, compensating for biases arising from high arterial concentrations of the contrast agent, inflow effects, and partial volume effects in the arterial AIF estimation ($C_b(t)$)^{25,31}.

Equation (5), integrating a Gaussian function and an exponential function modulated by a sigmoid function, was applied for curve fitting the first-pass component of the AIF, eliminating the influences of the second-pass circulation and venous blood flow²⁵.

$$C_b(t) = \frac{A}{\sigma\sqrt{2\pi}} e^{\left(\frac{-(t-T)^2}{2\sigma^2}\right)} + \alpha \frac{e^{-\beta t}}{(1 + e^{-s(t-\tau)})} \quad (5)$$

where A , T , and σ are the scaling constants, centers, and widths of the Gaussian function, respectively, α and β are the amplitudes and decay constants, respectively, of the exponential function, and s and τ are the width and center of the sigmoid function, respectively.

Calculation of signal-to-noise ratio (SNR) of AIF. The temporal SNR of the AIF is calculated according to the following equation:

$$SNR = \frac{C_{max}}{C_{baseline_SD}} \quad (6)$$

where C_{max} represents the maximal value of the AIF and $C_{baseline_SD}$ represents the standard deviation of the baseline of the AIF.

Simulations of AIFs with various peaks and time delays. By changing the peaks and delay times of a real aortic concentration time curve acquired from a given participant, AIFs were simulated to evaluate their influences on the perfusion parameters (K^{trans} , K_{ep} , v_e , and v_p). First, a typical AIF_A was generated from a chosen participant. Then, AIFs with various peaks were generated by rescaling the peak amplitude by factors of 1, 1/2, 1/4, and 1/6 (Fig. 4a). Similarly, AIFs with various delay times were generated by shifting the AIFs by 0, 1, 2, and 3 time points (Fig. 4b). A concentration time curve for the vertebra was acquired from the same participant, subsequently generating 1000 curves under each condition using the same SNR of 20 with random noise levels. Finally, the perfusion parameters from these 1000 curves were computed for each peak and delay times.

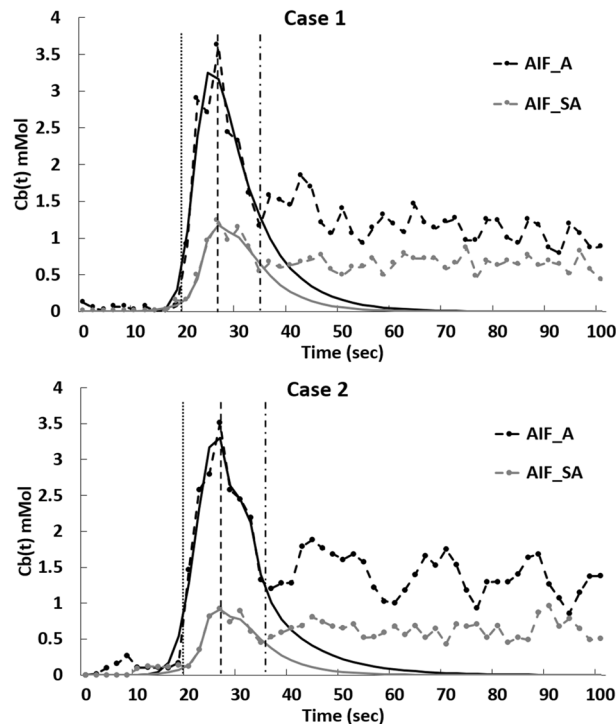


Figure 5. Concentration time curves and the corresponding first-pass fitted curves of the aorta and segmental artery of two participants. Dotted vertical lines represent the arrival of the first pass, dashed lines represent the peak, and dash-dotted lines represent the arrival of second pass of contrast-agent-containing blood. Black dashed curves represent the fit curves for the aortic arterial input function (AIF). Gray dashed curves represent the fit curves for the segmental arterial AIF.

Statistical analysis. Statistical analysis was performed by using SPSS software (IBM SPSS Statistics for Windows, Version 24.0; IBM Corp., Armonk, NY). The Wilcoxon signed rank test (WSRT) was used to compare the perfusion parameters between generated using a PWM and an RBM. The Mann–Whitney U test was used to compare the SNR of the concentration time curves of between the aorta and the segmental artery. The Kruskal–Wallis test (KWT) was used to compare the perfusion parameters generated using various AIFs and methods, applying a Dunn–Bonferroni post hoc correction across multiple comparisons. A P value less than 0.05 was considered to indicate statistical significance.

Results

The concentration time curves of the aorta and segmental arteries and the corresponding AIFs are shown in Fig. 5. The SNR (82.12 ± 30.81) of the aortic $Cb(t)$ was significantly higher than that (37.94 ± 23.42) of the segmental arterial $Cb(t)$ ($P < 0.01$). The transit time, defined as the interval between the arrival of the first pass and the arrival of second pass, remained consistent between the aortic and segmental arterial time curves. Data used for curve fitting the AIFs included the baseline, the upslope, and 3–4 data points after the peak in each concentration time curve, thus preventing contamination from the second pass (Fig. 5).

For every participant, the peak of AIF_A (5.04 ± 1.36 mmol; mean \pm standard deviation) was significantly greater than the peak of AIF_SA (1.81 ± 0.53 mmol) ($P < 0.001$). No differences were found between contrast arrival times (aorta, 16.5 ± 2.33 s; segmental artery, 17.8 ± 2.47 s; $P = 0.24$).

Perfusion parameters at various AIF peak amplitudes and delay times in the simulation are shown in Fig. 6. As the peak amplitude of the AIF decreased, both K^{trans} and v_e obviously increased, but neither K_{ep} nor v_p were affected. On the other hand, as the delay time of the AIF increased, v_p increased, but other perfusion parameters were not affected.

Perfusion parametric maps calculated from AIF_A and from AIF_SA for a randomly selected participant are shown in Fig. 7. Both K^{trans} and v_e were obviously lower in the lumbar vertebra when the perfusion parameters are calculated using AIF_A compared to AIF_SA.

The perfusion parameters obtained using PWM and RBM are shown in Fig. 8. Values for K^{trans} using AIF_PA (0.0159 ± 0.0053 min $^{-1}$ and 0.0156 ± 0.0055 min $^{-1}$, respectively) and AIF_A (0.0225 ± 0.0079 min $^{-1}$ and 0.0223 ± 0.0078 min $^{-1}$, respectively) were significantly lower ($P < 0.001$) than those using the AIF_SA (0.0679 ± 0.0316 min $^{-1}$ and 0.0578 ± 0.0219 min $^{-1}$, respectively). Likewise, v_e , determined using AIF_PA (0.1179 ± 0.0492 and 0.1253 ± 0.0509 , respectively) as well as AIF_A (0.1888 ± 0.1083 and 0.2003 ± 0.1099 , respectively) were significantly lower ($P < 0.01$) than those using AIF_SA (0.5296 ± 0.2241 and 0.5355 ± 0.2484 ,

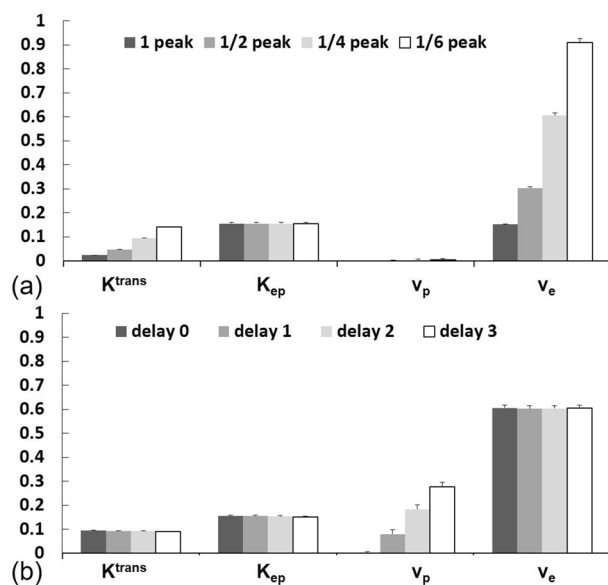


Figure 6. Perfusion parameters in a simulation study, varying (a) peaks and (b) delay times in the arterial input function.

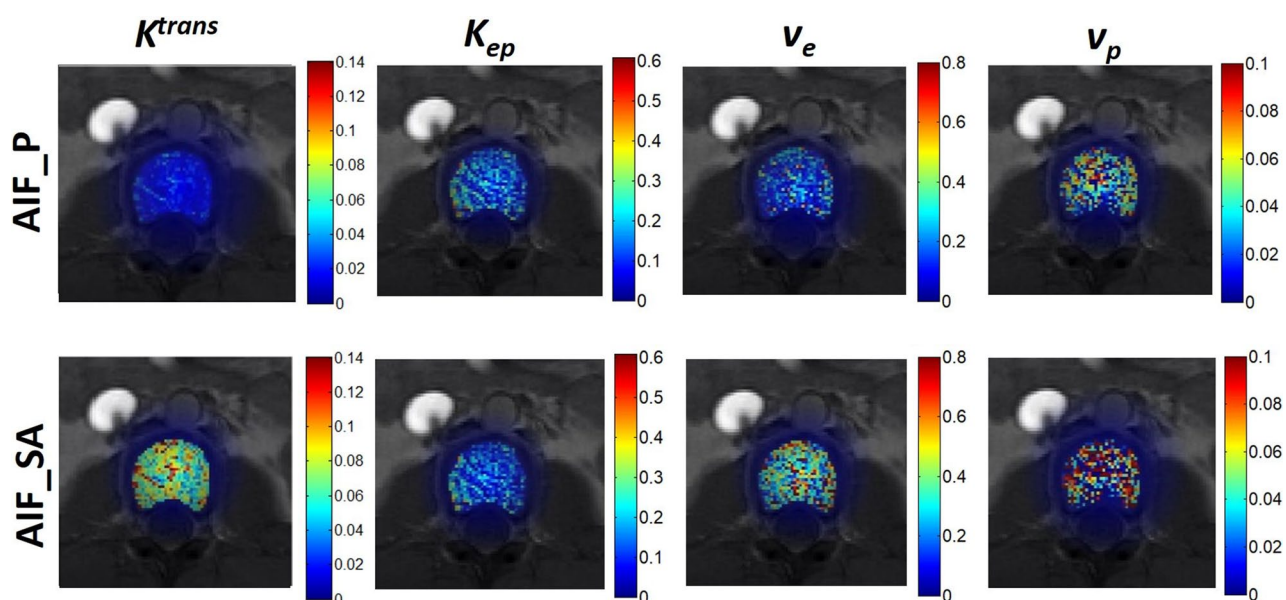


Figure 7. Maps of the perfusion parameters including K^{trans} , K_{ep} , v_e , and v_p for one participant, using an aortic arterial input function (AIF; top row) or a segmental arterial AIF (bottom row).

respectively). In particular, K^{trans} and v_e , calculated using AIF_SA, were greater than those using AIF_PA and AIF_A, no matter the computation method applied (Fig. 9).

The WSRT indicated that K^{trans} and K_{ep} , calculated using the PWM, were significantly greater than those calculated using the RBM (all $P < 0.005$), and that v_e , calculated using the PWM, was significantly lower than that calculated using the RBM (all $P < 0.01$), no matter the AIFs selected. Finally, v_p , if calculated using the PWM, was significantly greater than if calculated using the RBM (all $P < 0.05$), but only when AIF_SA was selected. On the other hand, the KWT did not indicate any significant differences between AIFs and computation methods when calculating any parameter except v_p , which was significantly ($P = 0.042$) greater using the PWM vs. the RBM when AIF_SA was selected.

Comparisons of the perfusion parameters calculated using PWM and RBM are shown in Table 1. In all AIFs, the WSRT indicates that K^{trans} and K_{ep} calculated using PWM were significantly greater than those found using RBM (all $P < 0.005$), but that values for v_e calculated by using PWM were significantly lower than those found using RBM (all $P < 0.01$). Only for AIF_SA did v_p significantly differ: it was significantly greater using

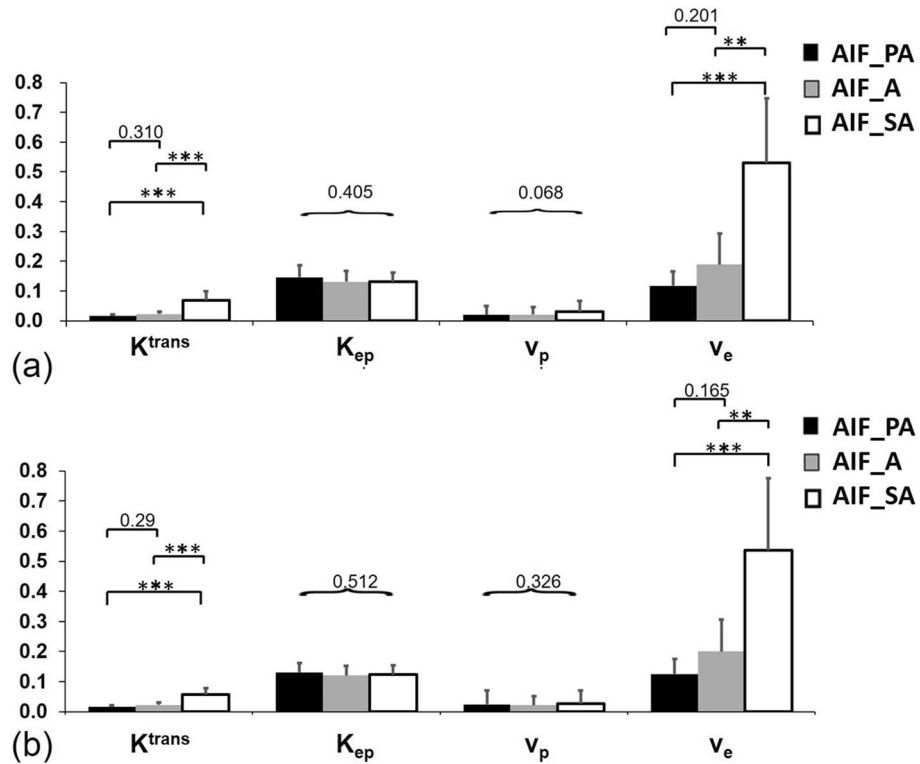


Figure 8. Comparing the perfusion parameters K^{trans} , K_{ep} , v_e , and v_p between the population-based (Parker) arterial input function (AIF; black), aortic AIF (gray) and segmental arterial AIF (white) using (a) a pixel-by-pixel computational method and (b) a region-of-interest computational method. Note: data are presented as means and standard deviations. ** $P < 0.01$, *** $P < 0.001$.

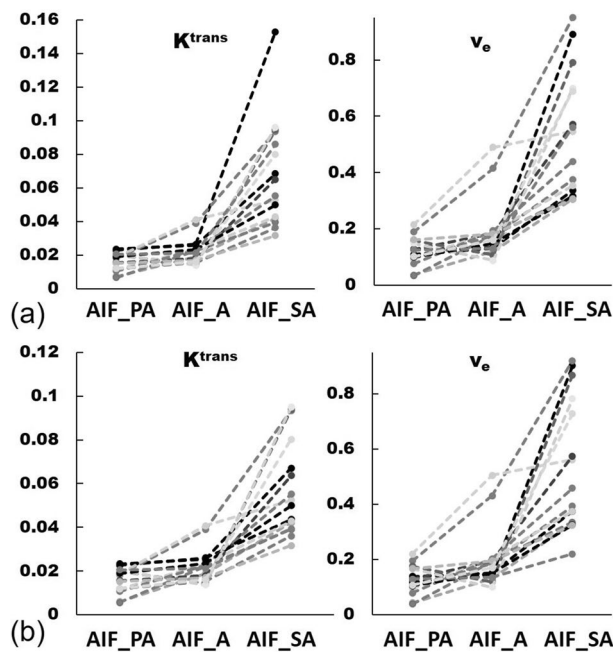


Figure 9. Values for K^{trans} and v_e calculated using the population-based (Parker) arterial input function (AIF), aortic AIF, and segmental arterial AIF in 16 vertebrae using a pixel-by-pixel method (a) and a region-of-interest method (b).

Parameters	Methods	AIF_P	AIF_A	AIF_SA
K_{trans} (min ⁻¹)	PWM	0.0159 ± 0.0053	0.0225 ± 0.0079	0.0679 ± 0.0316
	RBM	0.0156 ± 0.0055	0.0222 ± 0.0079	0.0578 ± 0.0219
	P value			
	WRST	***	***	***
	KWT	0.763	0.792	0.386
K_{ep} (min ⁻¹)	PWM	0.1462 ± 0.0418	0.1312 ± 0.0381	0.1314 ± 0.0320
	RBM	0.1310 ± 0.0314	0.1206 ± 0.0328	0.1244 ± 0.0308
	P value			
	WRST	***	***	***
	KWT	0.214	0.309	0.366
v_p	PWM	0.200 ± 0.0308	0.0203 ± 0.0271	0.0314 ± 0.0358
	RBM	0.241 ± 0.0481	0.0219 ± 0.0314	0.0267 ± 0.0455
	P value			
	WRST	0.326	0.679	*
	KWT	0.065	0.083	*
v_e	PWM	0.1179 ± 0.0493	0.1888 ± 0.1083	0.5296 ± 0.2242
	RBM	0.1253 ± 0.0509	0.2003 ± 0.1099	0.5355 ± 0.2485
	P value			
	WRST	***	***	**
	KWT	0.498	0.327	0.734

Table 1. Comparison of perfusion parameters between PWM and RBM regarding different AIFs. * $P < 0.05$, ** $P < 0.01$, *** $P < 0.001$.

PWM compared to RBM (all $P < 0.05$). On the other hand, the KWT showed no significant differences in any parameter except for v_p , which was significantly greater ($P = 0.042$) when PWM was used compared to RBM and only for AIF_SA.

Discussion

It is known that DCE-MRI is useful for detecting and characterizing tissue perfusion. The Tofts model is commonly used for quantitative analysis of DCE-MRI. To apply this model, AIF and the pre-contrast T1 value must be accurately measured¹. However, determining the AIF remains technically challenging because of the location of the upstream, slice orientation, partial volume, and flow artifacts. Studies have shown that AIF can have a large effect on the accuracy of computed pharmacokinetic parameters^{32–34}. Theoretically, a local AIF sampled at the inlet to the target tissue should be selected. In clinical practice, however, a major artery is often chosen instead, neglecting the effects of dispersion and delay of the AIF^{32,35}. Allowing evaluation of multiple vertebrae in a single slice, AIF_A measured on the sagittal plane has been widely used in vertebral perfusion studies^{8,15–17,36–39}. To the best of our knowledge, the effects of various AIFs on vertebral perfusion analysis has not yet been investigated.

In humans, each lumbar vertebra is supplied by a pair of segmental arteries which originate from the aorta^{18,19}. This study showed that an axial slice allows the aorta and segmental arteries to be simultaneously scanned in each slice (Fig. 3) and therefore provides a chance to examine the effects of various AIFs (i.e., AIF_A and AIF_SA) on vertebral perfusion quantification. By intentionally perturbing the amplitude and delay time of an AIF, we simulated the effects of arterial size and location of an AIF on perfusion parameter quantification. Results showed that K^{trans} and v_e are associated with the peak of the AIF and that v_p is associated with AIF delay time (Fig. 6). Conceptually, AIF_SA has a smaller peak and somewhat longer time delay compared to AIF_A, obtained from the adjacent aorta. Therefore, it is expected that K^{trans} and v_e , calculated using AIF_SA, would be greater than those found using AIF_A. As shown in Fig. 7, our perfusion parametric maps disclose relatively lower value for K^{trans} , v_e , and v_p in the lumbar vertebra when AIF_PA is used rather than AIF_SA. The results across 16 lumbar vertebrae in eight healthy people revealed similar trends in the simulation: K^{trans} and v_e were significantly greater when AIF_SA was used compared to AIF_A (Fig. 8).

The pros and cons of choosing axial slices in quantifying lumbar vertebral perfusion have not yet been explored. An axial slice allows AIF_A and AIF_SA to be simultaneously acquired, providing an opportunity to verify how each affects lumbar vertebral perfusion quantification. Nevertheless, selection of an axial slice has two drawbacks. First, only one vertebra can be viewed in each slice. To pursue a high temporal resolution of 2 s per dynamic phase, we acquired only two axial slices. When additional lumbar vertebrae are examined, lower temporal resolution and a longer acquisition time will be encountered when using axial slices. Sagittal and coronal slices allow the capture of multiple vertebrae in a single slice; however, they cannot provide the AIF_A and AIF_SA simultaneously. Notably, when scoliosis or malalignment of the lumbar spine is encountered, an attempt to acquire multiple vertebrae via sagittal or coronal slices, respectively, could result in limited success. Second, measures of AIF_SA on axial slices are susceptible to partial volume effects⁴⁰ and in-flow effects⁴¹. A thin slice can reduce the partial volume effects; nevertheless, a slice thickness of 10 mm provides a greater SNR

and a chance to include the entire course of the curving segmental artery in a single axial slice. To eliminate the in-flow pulsation on AIF_A, a pre-saturation band with parallel slices was applied on the upstream aorta. However, this pre-saturation band might also affect the calculation of peak concentration of the AIF, requiring further verification when applied.

Parker's model with a population-based flow-adapted fixed model and a correction AIF method was used as a reference^{25,30,42}. The AIFs were selected individually for each participant, then the peak concentration in the blood ($C_b(t)$) of the aorta was adjusted to 6 mmol in the population-based Parker model²⁵. Simulation results show that certain perfusion parameters are sensitive to the peak of contrast concentration in the blood. A comparison between three AIFs (AIF_PA, AIF_A, and AIF_SA) in vivo shows that all values for K^{trans} and v_e are significantly greater using AIF_SA compared to either AIF_PA or AIF_A. This might be attributable to a greater concentration in AIF_PA and AIF_A compared to AIF_SA. Given the fixed blood volume found in the vertebra, an AIF with a greater peak concentration, as seen in the aorta, will generate a lower blood transfer constant due to a greater blood volume in the aorta. This can explain why K^{trans} and v_e are lower at greater peak concentrations using AIF_A compared to AIF_SA, where peak concentrations are lower. Simulation results further show that v_p increases as delay time increases, but did not vary based on AIF selection. Differences in the results of simulations compared to human studies might be explained by insufficient time delays between the aorta and the segmental artery in the human studies.

This study has several limitations. First, a sample size of eight is small; however, the appropriate number of healthy volunteers should be carefully deliberated, give the risks of allergy, nephrotoxicity, neurotoxicity and potential nephrogenic systemic fibrosis, which must be considered together. We strictly followed the ethical principle to recruit the smallest number of healthy participants (to receive gadolinium-required DCE-MRI) possible while maintaining optimal power for statistical analysis. We similarly chose a minimal sample of participant for a previous study²⁰. This limitation was remedied by data augmentation: we chose two vertebrae from each participant, resulting in a pool of 16 vertebrae to examine. Furthermore, simulation results for perfusion parameters related to the peak concentration in the AIF are consistent with those from our human study. Second, only two lumbar vertebrae were scanned per participant, and only axial views were obtained. While axial images have the disadvantage of limited number of vertebrae examined, they outperform sagittal and coronal images in their ability to allow AIF_A and AIF_SA to be acquired simultaneously. Third, because of the thicker slice thickness than the diameter of segmental artery, partial volume has an effect not only on the AIF_SA theoretically but also the resulting pharmacokinetic parameters. We intentionally chose a slice thickness of 10 mm to increase the SNR in the DCE-MRI at a high temporal resolution of 2 s per dynamic phase and to include the entire course of the segmental artery in a single axial slice, knowingly risking partial volume effects. Problems caused by partial volume effects were partially remedied by applying subtracted DCE-MRI, thus providing dynamic images with improved SNRs that allowed easy detection of the segmental arteries. A single pixel centrally located in the artery and clearly demonstrating the first-pass peak within the ROI encompassing the segmental artery was chosen to fit the AIF_SA. By including data only from the baseline, upslope, peak, and 3 to 4 data points following the peak, only the first pass was used to fit AIF_SA. Nevertheless, further studies using various slice thicknesses are suggested to verify the partial volume effects on the measures of peak enhancement in AIF_SA. Fourth, AIF_A might be inherently influenced by the effects of in-flow enhancement on 2D axial images. Our remedy was to apply a pre-saturation band parallel to the slices of the acquired images on the upstream aorta and used the peak of AIF_PA as a correction. Quantitative evaluations of the in-flow enhancement effects on lumbar vertebral perfusion parameters are warranted. Fifth, we did not measure and did not correct for B1 field inhomogeneity. An uncorrected B1 field inhomogeneity is potentially a biasing factor; however, its influence is location specific, and the effects on perfusion parameters in a given location (e.g., the lumbar vertebrae) is time invariant. Therefore, its influence in a comparative study between AIFs, such as this study, is limited. Nevertheless, further studies would verify its effects on the quantification of lumbar perfusion parameters. Sixth, we enrolled only healthy participants and did not include patients with diseases of the lumbar vertebrae. Inclusion of those with disease was beyond the scope of this study, which was performed to test our hypothesis. In another study, we showed a 14% decrease in blood perfusion between two degenerated disks in the lumbar vertebra compared to two normal disks¹¹. A study designed to compare the lumbar vertebral perfusion parameters generated using PWM vs. RBM and using AIF_A vs. AIF_SA has been launched in the environment of degenerative lumbar disease. Finally, we did not evaluate the test–retest reliability nor inter-observer agreement. Further study is warranted to verify the robustness of our findings. Accordingly, the results of human experiments presented in this study were related to the selection of AIF solely based on the axial images. We suggest readers to notice the potential limitations of this study and not over-emphasize the absolute values of presented parameters while interpreting our experimental results.

In conclusion, the perfusion parameters K^{trans} and v_e in AIF_SA are significantly greater than those in AIF_A. Whether it is beneficial to simultaneously acquire both AIFs to quantify vertebral perfusion when using axial slice orientation deserves further verifying studies.

Data availability

The datasets generated during and/or analyzed during the current study are available from the corresponding author on reasonable request.

Received: 27 June 2020; Accepted: 19 January 2021

Published online: 03 February 2021

References

- Tofts, P. S. *et al.* Estimating kinetic parameters from dynamic contrast-enhanced T(1)-weighted MRI of a diffusable tracer: standardized quantities and symbols. *J. Magn. Reson. Imaging* **10**, 223–232. [https://doi.org/10.1002/\(SICI\)1522-2586\(199909\)10:3%3c223::AID-JMRI2%3e3.0.CO;2-S](https://doi.org/10.1002/(SICI)1522-2586(199909)10:3%3c223::AID-JMRI2%3e3.0.CO;2-S) (1999).
- Luybaert, R., Boujraf, S., Sourbron, S. & Osteaux, M. Diffusion and perfusion MRI: basic physics. *Eur. J. Radiol.* **38**, 19–27. [https://doi.org/10.1016/S0720-048X\(01\)00286-8](https://doi.org/10.1016/S0720-048X(01)00286-8) (2001).
- Cova, M. *et al.* Bone marrow perfusion evaluated with gadolinium-enhanced dynamic fast MR imaging in a dog model. *Radiology* **179**, 535–539 (1991).
- Fujisawa, K. *et al.* Value of a dynamic MR scan in predicting vascular ingrowth from free vascularized scapular transplant used for treatment of avascular femoral head necrosis. *Microsurgery* **16**, 673–678 (1995).
- Moehler, T. M. *et al.* Bone marrow microcirculation analysis in multiple myeloma by contrast-enhanced dynamic magnetic resonance imaging. *Int. J. Cancer* **93**, 862–868 (2001).
- Bollow, M. *et al.* Initial experience with dynamic MR imaging in evaluation of normal bone marrow versus malignant bone marrow infiltrations in humans. *J. Magn. Reson. Imaging* **7**, 241–250 (1997).
- Mouloupoulos, L. A. *et al.* Detection of malignant bone marrow involvement with dynamic contrast-enhanced magnetic resonance imaging. *Ann. Oncol.* **14**, 152–158 (2003).
- Hawighorst, H. *et al.* Evaluation of angiogenesis and perfusion of bone marrow lesions: role of semiquantitative and quantitative dynamic MRI. *J. Magn. Reson. Imaging* **10**, 286–294 (1999).
- Rahmouni, A. *et al.* Bone marrow with diffuse tumor infiltration in patients with lymphoproliferative diseases: dynamic gadolinium-enhanced MR imaging. *Radiology* **229**, 710–717 (2003).
- Fletcher, B. D., Hanna, S. L., Fairclough, D. L. & Gronemeyer, S. A. Pediatric musculoskeletal tumors: use of dynamic, contrast-enhanced MR imaging to monitor response to chemotherapy. *Radiology* **184**, 243–248 (1992).
- Liu, Y. J. *et al.* Intervertebral disk degeneration related to reduced vertebral marrow perfusion at dynamic contrast-enhanced MRI. *AJR Am. J. Roentgenol.* **192**, 974–979. <https://doi.org/10.2214/AJR.08.1597192/4/974> (2009).
- Griffith, J. F. *et al.* Vertebral marrow fat content and diffusion and perfusion indexes in women with varying bone density: MR evaluation. *Radiology* **241**, 831–838. <https://doi.org/10.1148/radiol.2413051858> (2006).
- Griffith, J. F. *et al.* Compromised bone marrow perfusion in osteoporosis. *J. Bone Miner. Res.* **23**, 1068–1075. <https://doi.org/10.1359/jbmr.080233> (2008).
- Khadem, N. R. *et al.* Characterizing hypervascular and hypovascular metastases and normal bone marrow of the spine using dynamic contrast-enhanced MR imaging. *AJNR Am. J. Neuroradiol.* **33**, 2178–2185. <https://doi.org/10.3174/ajnr.A3104> (2012).
- Biffar, A. *et al.* Quantitative analysis of vertebral bone marrow perfusion using dynamic contrast-enhanced MRI: initial results in osteoporotic patients with acute vertebral fracture. *J. Magn. Reson. Imaging* **33**, 676–683. <https://doi.org/10.1002/jmri.22497> (2011).
- Chu, S. *et al.* Measurement of blood perfusion in spinal metastases with dynamic contrast-enhanced magnetic resonance imaging: evaluation of tumor response to radiation therapy. *Spine (Phila Pa 1976)* **38**, E1418–1424. <https://doi.org/10.1097/BRS.0b013e3182a40838> (2013).
- Lis, E. *et al.* Dynamic contrast-enhanced magnetic resonance imaging of osseous spine metastasis before and 1 hour after high-dose image-guided radiation therapy. *Neurosurg. Focus* **42**, E9. <https://doi.org/10.3171/2016.9.FOCUS16378> (2017).
- Crock, H. V. & Yoshizawa, H. *1 Online Resource(xiii)* 130 (Springer, New York, 1977).
- Shimizu, S. *et al.* Origins of the segmental arteries in the aorta: an anatomic study for selective catheterization with spinal arteriography. *AJNR Am. J. Neuroradiol.* **26**, 922–928 (2005).
- Chiu, S. C. *et al.* Influence of amplitude-related perfusion parameters in the parotid glands by non-fat-saturated dynamic contrast-enhanced magnetic resonance imaging. *Med. Phys.* **43**, 1873. <https://doi.org/10.1118/1.4943798> (2016).
- Wang, H. Z., Riederer, S. J. & Lee, J. N. Optimizing the precision in T1 relaxation estimation using limited flip angles. *Magn. Reson. Med.* **5**, 399–416 (1987).
- Rohrer, M., Bauer, H., Mintonovitch, J., Requardt, M. & Weinmann, H. J. Comparison of magnetic properties of MRI contrast media solutions at different magnetic field strengths. *Investig. Radiol.* **40**, 715–724. <https://doi.org/10.1097/01.rli.0000184756.66360.d3> (2005).
- Tofts, P. S. Modeling tracer kinetics in dynamic Gd-DTPA MR imaging. *J. Magn. Reson. Imaging* **7**, 91–101 (1997).
- Leach, M. O. *et al.* Imaging vascular function for early stage clinical trials using dynamic contrast-enhanced magnetic resonance imaging. *Eur. Radiol.* **22**, 1451–1464. <https://doi.org/10.1007/s00330-012-2446-x> (2012).
- Parker, G. J. *et al.* Experimentally-derived functional form for a population-averaged high-temporal-resolution arterial input function for dynamic contrast-enhanced MRI. *Magn. Reson. Med.* **56**, 993–1000. <https://doi.org/10.1002/mrm.21066> (2006).
- Cardenas-Rodriguez, J., Howison, C. M., Matsunaga, T. O. & Pagel, M. D. A reference agent model for DCE MRI can be used to quantify the relative vascular permeability of two MRI contrast agents. *Magn. Reson. Imaging* **31**, 900–910. <https://doi.org/10.1016/j.mri.2012.12.002> (2013).
- Cardenas-Rodriguez, J., Howison, C. M. & Pagel, M. D. A linear algorithm of the reference region model for DCE-MRI is robust and relaxes requirements for temporal resolution. *Magn. Reson. Imaging* **31**, 497–507. <https://doi.org/10.1016/j.mri.2012.10.008> (2013).
- DeGrandchamp, J., & Cárdenas-Rodríguez, J. *fitdcmri: A Matlab Function for the Analysis of DCE MRI Data*. <https://osf.io/tmj5b/> (2016).
- Lee, J. *et al.* Comparison of analytical and numerical analysis of the reference region model for DCE-MRI. *Magn. Reson. Imaging* **32**, 845–853. <https://doi.org/10.1016/j.mri.2014.04.007> (2014).
- Singh, A. *et al.* Improved bolus arrival time and arterial input function estimation for tracer kinetic analysis in DCE-MRI. *J. Magn. Reson. Imaging* **29**, 166–176. <https://doi.org/10.1002/jmri.21624> (2009).
- Chikui, T. *et al.* The principal of dynamic contrast enhanced MRI, the method of pharmacokinetic analysis, and its application in the head and neck region. *Int. J. Dent.* **2012**, 480659. <https://doi.org/10.1155/2012/480659> (2012).
- Sourbron, S. P. & Buckley, D. L. Classic models for dynamic contrast-enhanced MRI. *NMR Biomed.* **26**, 1004–1027. <https://doi.org/10.1002/nbm.2940> (2013).
- Huang, W. *et al.* The impact of arterial input function determination variations on prostate dynamic contrast-enhanced magnetic resonance imaging pharmacokinetic modeling: a multicenter data analysis challenge. *Tomography* **2**, 56–66. <https://doi.org/10.18383/j.tom.2015.00184> (2016).
- Mehrtash, A. *et al.* Bolus arrival time and its effect on tissue characterization with dynamic contrast-enhanced magnetic resonance imaging. *J. Med. Imaging (Bellingham)* **3**, 014503. <https://doi.org/10.1117/1.JMI.3.1.014503> (2016).
- Calamante, F. Arterial input function in perfusion MRI: a comprehensive review. *Prog. Nucl. Magn. Reson. Spectrosc.* **74**, 1–32. <https://doi.org/10.1016/j.pnmrs.2013.04.002> (2013).
- Kanchiku, T., Taguchi, T., Toyoda, K., Fujii, K. & Kawai, S. Dynamic contrast-enhanced magnetic resonance imaging of osteoporotic vertebral fracture. *Spine (Phila Pa 1976)* **28**, 2522–2526. <https://doi.org/10.1097/01.BRS.0000092384.29767.85> (2003).
- Shih, T. T. *et al.* Correlation of MR lumbar spine bone marrow perfusion with bone mineral density in female subjects. *Radiology* **233**, 121–128. <https://doi.org/10.1148/radiol.2331031509> (2004).

38. Montazel, J. L. *et al.* Normal spinal bone marrow in adults: dynamic gadolinium-enhanced MR imaging. *Radiology* **229**, 703–709. <https://doi.org/10.1148/radiol.2293020747> (2003).
39. Griffith, J. F. *et al.* Vertebral bone mineral density, marrow perfusion, and fat content in healthy men and men with osteoporosis: dynamic contrast-enhanced MR imaging and MR spectroscopy. *Radiology* **236**, 945–951. <https://doi.org/10.1148/radiol.2363041425> (2005).
40. van Osch, M. J., van der Grond, J. & Bakker, C. J. Partial volume effects on arterial input functions: shape and amplitude distortions and their correction. *J. Magn. Reson. Imaging* **22**, 704–709. <https://doi.org/10.1002/jmri.20455> (2005).
41. Peeters, F., Annet, L., Hermoye, L. & Van Beers, B. E. Inflow correction of hepatic perfusion measurements using T1-weighted, fast gradient-echo, contrast-enhanced MRI. *Magn. Reson. Med.* **51**, 710–717. <https://doi.org/10.1002/mrm.20032> (2004).
42. Parker, G. J., Waterton, J. C., & Buckley, D. L. In *Proceedings of the 11th Annual Meeting of ISMRM*. p 1264.

Acknowledgements

Yi-Jui Liu, Shao-Chieh Lin, and Chun-Jung Juan received funding support from the Taiwan Ministry of Science and Technology (107-2221-E-035 -033 -MY3). Wing P. Chan received funding support from the Taiwan Ministry of Science and Technology (MOST103-2320-B038-005-MY3) and Wan Fang Hospital, Taipei Medical University (Grant No.: 105swf08). Chun-Jung Juan, Wu-Chung Shen and Der-Yang Cho received funding support from the China Medical University Hospital (Grant No.: CMUH-DMR-108-056).

Author contributions

Y.-J.L., C.-J.J., and W.P.C. contributed to the conception or design of the work. M.M.Y., H.-T.Y. and W.P.C. contributed to the acquisition of the data, Y.-J.L., S.-C.L., D.-Y.C., W.-C.S. and C.-J.J. contributed to the analysis and interpretation of data for the work. Y.-J.L. and C.-J.J. drafted the manuscript. All authors have approved the final version to be published.

Competing interests

The authors declare no competing interests.

Additional information

Correspondence and requests for materials should be addressed to C.-J.J. or W.P.C.

Reprints and permissions information is available at www.nature.com/reprints.

Publisher's note Springer Nature remains neutral with regard to jurisdictional claims in published maps and institutional affiliations.



Open Access This article is licensed under a Creative Commons Attribution 4.0 International License, which permits use, sharing, adaptation, distribution and reproduction in any medium or format, as long as you give appropriate credit to the original author(s) and the source, provide a link to the Creative Commons licence, and indicate if changes were made. The images or other third party material in this article are included in the article's Creative Commons licence, unless indicated otherwise in a credit line to the material. If material is not included in the article's Creative Commons licence and your intended use is not permitted by statutory regulation or exceeds the permitted use, you will need to obtain permission directly from the copyright holder. To view a copy of this licence, visit <http://creativecommons.org/licenses/by/4.0/>.

© The Author(s) 2021